



# Linkage effect in the bandgap-broken $V_2O_5$ -GdCrO<sub>3</sub> heterojunction by carbon allotropes for boosting photocatalytic H<sub>2</sub> production

Jingwei Li<sup>a</sup>, Zhengyi Huang<sup>a,c</sup>, Cong Wang<sup>b,f</sup>, Lei Tian<sup>a</sup>, Xiaoqing Yang<sup>d</sup>, Rongfu Zhou<sup>e</sup>, Mohamed Nawfal Ghazzal<sup>b</sup>, Zhao-Qing Liu<sup>a,\*</sup>

<sup>a</sup> School of Chemistry and Chemical Engineering/Institute of Clean Energy and Materials/Guangzhou Key Laboratory for Clean Energy and Materials/Huangpu Hydrogen Innovation Center, Guangzhou University, Guangzhou Higher Education Mega Center, No. 230 Wai Huan Xi Road, Guangzhou 510006, China

<sup>b</sup> Université Paris-Saclay, UMR 8000 CNRS, Institut de Chimie Physique, Orsay 91405, France

<sup>c</sup> School of Chemistry and Chemical Engineering of Hainan Normal University, Key Laboratory of Electrochemical Energy Storage and Energy Conversion of Hainan Province, Key Laboratory of Electrochemical Energy Storage and Light Energy Conversion Materials of Haikou City, Haikou 571158, China

<sup>d</sup> Shenzhen International Graduate School, Tsinghua University, Shenzhen 518055, China

<sup>e</sup> School of Environmental and Chemical Engineering, Foshan University, Foshan 528225, China

<sup>f</sup> Bingtuan Energy Development Institute, Shihezi University, No. 280 Beisi Road, Shihezi City, Xinjiang Uygur Autonomous Region 832000, China

## ARTICLE INFO

### Keywords:

Linkage effect  
Bandgap-broken heterojunction  
Carriers transfer  
Photocatalytic H<sub>2</sub> generation

## ABSTRACT

Refining carrier transfer in bandgap-broken heterojunctions, which consist of two semiconductors with broken bandgaps, is crucial yet highly challenging for photocatalysis. Herein, we incorporated amorphous carbons (AC) into the bandgap-broken  $V_2O_5$ /GdCrO<sub>3</sub> heterojunctions, inducing a linkage effect to facilitate photoexcited carrier transfer. The created V-O-C and Cr-O-C bonds in  $V_2O_5$ -AC-GdCrO<sub>3</sub> interfaces show almost identical orbital energies to overcome the broken-gap energy barriers at interfaces. The holes at GdCrO<sub>3</sub>'s valence band and electrons at  $V_2O_5$ 's conduction band tend to migrate toward the carbon ring of amorphous carbon via Cr-O-C and V-O-C bonds, thereby enhancing carrier separation of bandgap-broken  $V_2O_5$ /AC/GdCrO<sub>3</sub> heterojunction. By controlling the relative amount of metal-O-C bonds in the interface, the modulation of charge transfer kinetics was also achieved on  $V_2O_5$ /AC/GdCrO<sub>3</sub>, resulting in ~7 times higher of H<sub>2</sub> generation than  $V_2O_5$ /GdCrO<sub>3</sub>. The concept could be expanded to the other carbon allotropes, including graphene, carbon nanotube, and graphdiyne conjugated structures, demonstrating a universal strategy in reaching optimal charge transfer of broken-bandgap heterojunctions for photocatalytic H<sub>2</sub> production.

## 1. Introduction

Heterojunctions have been recognized as promising catalysts for photocatalytic hydrogen production [1]. The bandgap-overlapped heterojunctions (such as Z-scheme, S-scheme, and Type II) were extensively investigated for over 50 years in the context of photo(electro)catalytic H<sub>2</sub> production due to their efficient separate charge carrier and superior performance [2,3]. However, the overlapping bandgap of these materials results in a trade-off between light absorption range and band potentials, constraining their optimal performance. This restriction to bandgap-overlapped heterojunctions highlights the need to explore other types of materials. In this context, bandgap-broken heterojunctions, such as Type III and Type III-V, can easily achieve high photoredox potentials and wide-range optical absorption, which offer an

alternative to overcome the associated drawbacks of bandgap-overlapped heterojunctions [3–5]. They can be widely used in physical field to construct Esaki diodes, field effect transistors, et al., taking advantage of their charge transport in bandgap-broken interface via inter-band quantum tunneling assisted by bias voltage [4–6]. Nevertheless, achieving efficient carrier transfer in bandgap-broken heterojunctions is exceedingly challenging without the aid of bias voltage due to the energy barrier at interfaces. Accordingly, it is reasonable to speculate that the application potential of bandgap-broken heterojunction for photocatalytic H<sub>2</sub> production will be activated if efficient carrier transfer in bandgap-broken interfaces is achieved at room temperature without the assistance of bias voltage.

We previously introduced plasmonic metals (e.g. Ag, Bi) or plasmonic semiconductors ( $WO_{3-x}$ ) into interfaces to construct bandgap-

\* Corresponding author.

E-mail address: [lzqzu@gzhu.edu.cn](mailto:lzqzu@gzhu.edu.cn) (Z.-Q. Liu).

<https://doi.org/10.1016/j.apcatb.2023.123181>

Received 30 June 2023; Received in revised form 5 August 2023; Accepted 15 August 2023

Available online 23 August 2023

0926-3373/© 2023 Elsevier B.V. All rights reserved.

broken heterojunctions  $\text{Ag}_3\text{PO}_4/\text{Ag}/\text{GdCrO}_3$ ,  $\text{WO}_{3-x}/\text{GdCrO}_3$  or  $\text{Bi}/\text{Bi}_2\text{S}_3/\text{Bi}/\text{MnO}_2/\text{MnO}_x$  [7–9]. The photoexcited hot electron-hole pairs on those plasmonic materials transit to higher energy levels under photothermal conditions, and surmount the broken-gap energy barriers at interfaces, thereby enhancing carrier migration and separation for the bandgap-broken heterojunctions. This improved carrier separation efficiency leads to optimized photo(thermal)catalytic performance of those bandgap-broken heterojunctions for the degradation of volatile organic compounds (VOCs). However, the low hot electron-hole pairs generation efficiency of plasmonic metals/semiconductors or limited interacted areas between components at interfaces still restrict the optimized space for carriers transfer at bandgap-broken interfaces. Recently, interfacial chemical bonds have received much more attention for their capability to regulate the charge migration at atomic level at interfaces. The construction of chemical W–N bonds within a Z-scheme  $\text{g-C}_3\text{N}_4/\text{WO}_3$  heterojunction, In–O–Cd bonds in  $\text{In}_2\text{O}_3/\text{CdSe-DETA}$ , and C–S bond in  $\text{Bi}_{19}\text{S}_{27}\text{Br}_3/\text{g-C}_3\text{N}_4$  accelerated photogenerated charge transfer and optimized the photocatalytic activity [10–12]. However, constructing chemical bonds to fulfill the broken-gap energy barriers at interfaces and regulate the interfacial carriers's transfer in bandgap-broken heterojunctions still need to be elucidated.

In this work, we introduce amorphous carbon (AC) into a bandgap-broken interface, which is composed of  $\text{V}_2\text{O}_5$  (oxidation semiconductor [13,14]) and  $\text{GdCrO}_3$  (reduction semiconductor [7,8]). Both experimental and DFT calculation results indicate that the amorphous carbon in bandgap-broken  $\text{V}_2\text{O}_5$ – $\text{GdCrO}_3$  interfaces shows a linkage effect for carrier transfer and photocatalytic hydrogen reaction. The metal–O–C bonds as Cr–O–C (Cr 3d/O 2p/C 2p) and V–O–C (V 3d/O 2p/C 2p) bonds have been created at the  $\text{V}_2\text{O}_5$ – $\text{GdCrO}_3$  interfaces, which has virtually equal energy levels to overcome the broken-gap energy barriers of interfaces. In addition, the holes localized at Cr 3d orbitals of the  $\text{GdCrO}_3$  valence band and electrons on V 3d orbitals of  $\text{V}_2\text{O}_5$  conduction band migrate to carbon rings in amorphous carbon via Cr–O–C and V–O–C bonds, further optimize carrier migration and separation. The amorphous carbon layer (AC-L) has larger interacted area with semiconductors compared to amorphous carbon nanoparticles (AC-P) thereby possess a higher amount of metal–O–C bonds at interfaces. Impressively, the constructed VO/AC-L/GCO demonstrates superior charge transfer kinetics, resulting in exceptional photocatalytic  $\text{H}_2$  production, with a rate ( $1.86 \text{ mmol g}^{-1} \text{ h}^{-1}$ )  $\sim 7$  times greater than  $\text{V}_2\text{O}_5/\text{GdCrO}_3$  (VO/GCO).

## 2. Experiment section

### 2.1. Chemicals and reagents

Chromium (III) nitrate nonahydrate ( $\text{Cr}(\text{NO}_3)_3 \cdot 9 \text{H}_2\text{O}$ , AR), urea ( $\text{CON}_2\text{H}_4$ , AR), glucose ( $\text{C}_6\text{H}_{12}\text{O}_6$ , AR), ammonium metavanadate ( $\text{NH}_4\text{VO}_3$ , AR), and citric acid monohydrate ( $\text{C}_6\text{H}_8\text{O}_7 \cdot \text{H}_2\text{O}$ , AR), tetrahydrofuran (THF), N,N-Dimethylformamide (DMF), ethyl acetate (EA), tetrabutylammonium fluoride (TBAF, 1 M in THF), pyridine, acetone, hydrochloric acid (HCl), sodium chloride (NaCl, AR) and sodium sulfate ( $\text{Na}_2\text{SO}_4$ , AR) were purchased from Aladdin. Gadolinium nitrate hexahydrate ( $\text{Gd}(\text{NO}_3)_3 \cdot 6 \text{H}_2\text{O}$ ) was procured from Macklin. The graphene (GN) and multi-walled carbon nanotubes (CNT) were purchased from Guangdong Nanhai Prius Technology Co. LTD and Shenzhen Nanotech Port Co. Ltd., respectively. Hexakis [(trimethylsilyl) ethynyl] benzene (HEB-TMS) was purchased from Nanjing XFNANO Materials Tech Co., Ltd.). All chemicals were used directly without additional processing.

### 2.2. Synthesis of $\text{GdCrO}_3$ , VO/AC-P/GCO, VO/AC-L/GCO, VO/GCO, and $\text{V}_2\text{O}_5$

The  $\text{GdCrO}_3$  was synthesized via a calcination method. 7.21 g  $\text{CON}_2\text{H}_4$ , 4.0 g  $\text{Cr}(\text{NO}_3)_3 \cdot 9 \text{H}_2\text{O}$ , and 4.51 g  $\text{Gd}(\text{NO}_3)_3 \cdot 6 \text{H}_2\text{O}$  were homogeneously blended and calcinated under air atmosphere at  $850^\circ\text{C}$  for

3 h. The as-synthesized 0.2 g  $\text{GdCrO}_3$  was uniformly dispersed in 60 mL glucose water solutions, which were subsequently transferred into Teflon-lined stainless-steel autoclaves and heated at  $180^\circ\text{C}$  for 3 h. To achieve controlled synthesis of amorphous carbon nanoparticles/ $\text{GdCrO}_3$  (AC-P/GCO) and amorphous carbon layer/ $\text{GdCrO}_3$  (AC-L/GCO), the concentrations of the above glucose water solutions were adjusted to  $0.37 \text{ mol L}^{-1}$  and  $1.48 \text{ mol L}^{-1}$ , respectively. Then, 0.1 g of AC-P/GCO or AC-L/ $\text{GdCrO}_3$  was uniformly dispersed in 60 mL deionized water containing 0.11 g  $\text{C}_6\text{H}_8\text{O}_7 \cdot \text{H}_2\text{O}$  and 0.059 g  $\text{NH}_4\text{VO}_3$ . The resulting mixtures were transferred into Teflon-lined stainless-steel autoclaves and heated at  $180^\circ\text{C}$  for 12 h. The powders were collected, dried at  $80^\circ\text{C}$ , and calcinated at  $350^\circ\text{C}$  for 1.5 h under air atmosphere to obtain  $\text{V}_2\text{O}_5/\text{AC-P}/\text{GdCrO}_3$  (VO/AC-P/GCO) and  $\text{V}_2\text{O}_5/\text{AC-L}/\text{GdCrO}_3$  (VO/AC-L/GCO).

The  $\text{V}_2\text{O}_5/\text{GdCrO}_3$  (VO/GCO) was prepared through the similar processes of VO/AC-L/GCO except that no process of hydrothermal treatment applied between  $\text{GdCrO}_3$  and glucose. The synthesis of  $\text{V}_2\text{O}_5$  was achieved via the aforementioned VO/GCO processes without the addition of  $\text{GdCrO}_3$  powders.

### 2.3. Synthesis of GDY

The graphdiyne (GDY) was synthesized through the reported methods [15]. Typically, 50 mg HEB-TMS and 0.5 mL TBAF were added in 15 mL THF under  $\text{N}_2$  atmosphere and stirred at  $0^\circ\text{C}$  for 15 min. Then, the solution was diluted with EA and washed with brine and dried with anhydrous  $\text{Na}_2\text{SO}_4$ . The solvent was removed in vacuo and the deprotected material was further diluted with 20 mL pyridine and added slowly to a solution of copper foils in 30 mL pyridine. Then, the mixture was kept under  $\text{N}_2$  atmosphere at  $60^\circ\text{C}$  for 4 d. After completion, black films were obtained on the copper foils. The copper foils were washed with acetone and DMF in turn. The powder product was obtained through sonication, then washed with 1 M HCl, water and acetone. Afterward, the black GDY powder was collected through centrifugation and dried in oven overnight.

### 2.4. Synthesis of VO/GN/GCO, VO/CNT/GCO, VO/GDY/GCO

The VO/GN/GCO, VO/CNT/GCO, and VO/GDY/GCO heterojunctions were synthesized through hydrothermal treatment. In brief, 20 mg  $\text{V}_2\text{O}_5$ , 40 mg  $\text{GdCrO}_3$ , and 5 mg carbon allotrope (GN, CNT or GDY) were uniformly dispersed in 10 mL methanol using sonication (1 h) and vigorous stirring (30 min). The resulting mixtures were then transferred to Teflon-lined stainless-steel autoclaves and heated at  $180^\circ\text{C}$  for 12 h. Finally, the as-obtained powders were dried at  $80^\circ\text{C}$ .

### 2.5. Characterizations

The crystal structures and chemical states of materials were analyzed by PANalytical X-ray diffraction (XRD) apparatus, laser Raman spectrometer (LabRAM HR Evolution), Fourier transform infrared spectrometer (FTIR, PerkinElmer, Spectrum100), and X-ray photoelectron spectroscopy (XPS, Thermo Scientific K-Alpha). The morphology of samples was observed by emission scanning electron microscopy (SEM, Quanta 400 F) and transmission electron microscopy (TEM, JEOL JEM-2100 F). The optical properties were characterized using an ultraviolet-visible (UV–vis) diffuse reflectance spectrophotometer (DRS, UV-3600). Photoluminescence (PL) spectra and Time-resolved photoluminescence (TRPL) spectra were used to evaluate the charge carrier dynamics using Steady-state/Transient state fluorescence spectrometer (FLSP980). The TRPL spectra were fitted according to Eq. (1) and the average decay times ( $\tau_{\text{ave}}$ ) of photoexcited carriers were calculated using Eq. (2) [9,16]:

$$I(t) = A_1 e^{(-t/\tau_1)} + A_2 e^{(-t/\tau_2)} + A_3 e^{(-t/\tau_3)} \quad (1)$$

$$\tau_{\text{ave}} = (A_1 \tau_1^2 + A_2 \tau_2^2 + A_3 \tau_3^2) / (A_1 \tau_1 + A_2 \tau_2 + A_3 \tau_3) \quad (2)$$

Where  $A_1$ ,  $A_2$ , and  $A_3$  are the pre-exponential factors,  $\tau_1$  represents the free excitation from recombination of the photoexcited electron-hole pairs, and  $\tau_2$  and  $\tau_3$  are related to the nonradiative recombination at

the surfaces or interfaces. The photoelectrochemical properties were assessed using a three-electrode electrochemical setup (CHI660E) coupled with a Xe lamp. Sample powders were smeared on the FTO as the working electrodes.  $1.0 \text{ mol L}^{-1}$  of  $\text{Na}_2\text{SO}_4$  (pH = 7.0), and the Hg/

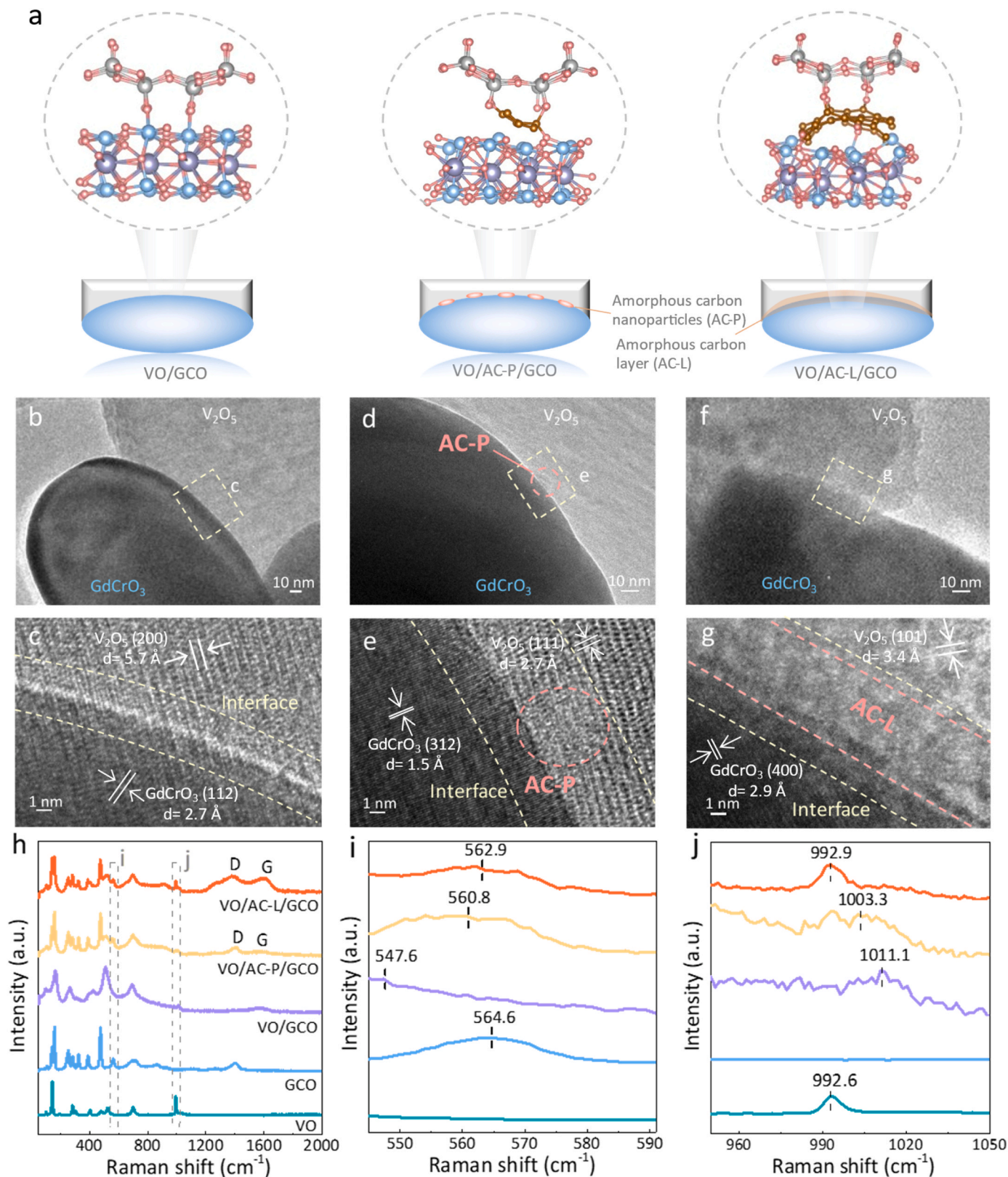


**Fig. 1.** (a) The structure schematic diagrams of heterojunctions. TEM and HRTEM images of (b, c) VO/GCO, (d, e) VO/AC-P/GCO and (f, g) VO/AC-L/GCO. (h) Raman spectra of samples and (i, j) the corresponding enlarged regions.



Hg<sub>2</sub>Cl<sub>2</sub> electrode were used as electrolytes for the reference electrodes, respectively. The flat-band potential ( $E_{fb}$ ) values obtained from Mott-Schottky (M-S) plots were adjusted using Eq. (3):

$$E_{fb} = E_{Hg/Hg_2Cl_2} + 0.242 \quad (3)$$

Where  $E_{fb}$  and  $E_{Hg/Hg_2Cl_2}$  refer to the potentials vs. Normal Hydrogen Electrode (NHE, pH = 7.0) and Hg/Hg<sub>2</sub>Cl<sub>2</sub> electrode, respectively.

## 2.6. DFT calculations

DFT calculations were performed using the projector-augmented wave method within the Vienna ab initio Simulation Package (VASP). The Perdew-Burke-Ernzerhof (PBE) functional in the generalized gradient approximation was employed as the exchange-correlation functional. A Hubbard U value of 3.7 eV was used to explain the strong correlation interaction between Cr 3d orbitals. The Brillouin zone was sampled using a  $2 \times 2 \times 1$  K-point mesh for surface calculations. A cutoff energy of 500 eV was employed, and structure relaxation was carried out until the convergence criteria for energy and force reached values of  $1 \times 10^{-4}$  eV and  $0.03 \text{ eV } \text{\AA}^{-1}$ , respectively. A vacuum layer of thickness 15 Å is introduced to eliminate interactions between periodic structures in the surface model.

## 2.7. Photocatalytic hydrogen generation

To evaluate photocatalytic hydrogen generation performance, the powders were dispersed in a 50 mL aqueous solution containing  $0.1 \text{ mol L}^{-1}$  NaS<sub>2</sub> –Na<sub>2</sub>SO<sub>3</sub> under ultrasonic and followed by stirring. Then, 1 wt% Pt co-catalysts were loaded onto the surface of the photocatalysts using a photoreduction of a solution containing H<sub>2</sub>PtCl<sub>6</sub> precursor. The mixture was then transferred to a 160 mL quartz photocatalytic reactor and bubbled with N<sub>2</sub> for 30 min to remove dissolved O<sub>2</sub>. The H<sub>2</sub> generated under was followed via Agilent 8860 GC over time irradiation by a Xe lamp (300 W).

## 3. Results and discussion

### 3.1. Synthesis, morphology, crystal phase and electronic states

Broken-gap heterojunctions, namely, V<sub>2</sub>O<sub>5</sub>/GdCrO<sub>3</sub> (VO/GCO), V<sub>2</sub>O<sub>5</sub>/amorphous carbon nanoparticles/GdCrO<sub>3</sub> (VO/AC-P/GCO) and V<sub>2</sub>O<sub>5</sub>/amorphous carbon layer/GdCrO<sub>3</sub> (VO/AC-L/GCO) were synthesized by combining following steps of hydrothermal treatments and calcination (Fig. 1a and Fig. S1). The reaction between GdCrO<sub>3</sub> and VO<sup>3+</sup> ions create a VO/GCO heterojunction (Fig. S1). In order to regulate the interacted areas between amorphous carbon V<sub>2</sub>O<sub>5</sub>, and GdCrO<sub>3</sub> at V<sub>2</sub>O<sub>5</sub>-AC-GdCrO<sub>3</sub> interfaces, the amorphous carbon nanoparticles

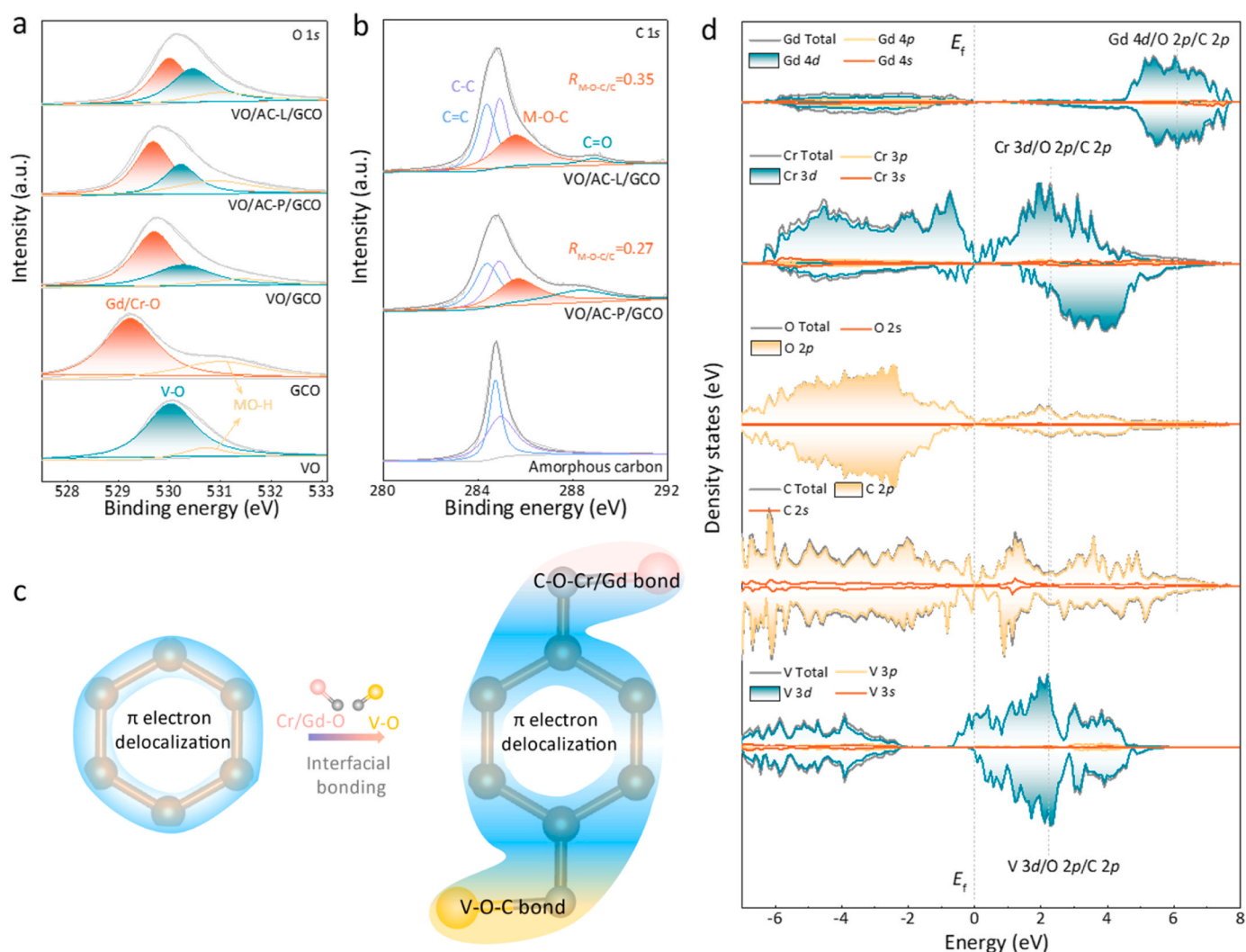


**Fig. 2.** (a) O 1s and (b) C 1s XPS spectra for samples. M refers to V, Gd or Cr. (c) The schematic diagram of  $\pi$  delocalized electrons on carbon ring of amorphous carbon before and after Cr/Gd-O, V-O bonds connecting. (d) The total and partial DOS (PDOS) spectra of Gd, Cr, O, C, V in VO/AC-L/GCO.

(AC-P/GCO) and an amorphous carbon layer (AC-L/GCO) were firstly grown on surfaces of  $\text{GdCrO}_3$  by controlling the reactive amount of glucose. Then,  $\text{VO}^{3+}$  ions were added to complete the formation of VO/AC-P/GCO and VO/AC-L/GCO heterojunctions (Fig. S1).

The SEM and TEM images of  $\text{GdCrO}_3$  reveal ellipsoidal-like nanoparticle with a large size distribution ranging from 100 to 600 nm (Fig. S2a). By adjusting the concentration of glucose during synthesis process, we could control the growth of amorphous carbon nanoparticles and amorphous carbon layer on the surface of  $\text{GdCrO}_3$  (Figs. S2b and 2c). The AC-P obtained at low glucose concentration exhibits a size of  $\sim 20$  nm, while a thin AC-L is formed at higher concentration. Furthermore, the pure  $\text{V}_2\text{O}_5$  shows a nanosheet structure (Fig. S2d). After combined with  $\text{GdCrO}_3$  to format VO/GCO heterojunction, the  $\text{GdCrO}_3$  nanoparticles are in contact with  $\text{V}_2\text{O}_5$  nanosheets (Fig. S3). Interestingly, introducing amorphous carbon into the VO-GCO.

interface does not alter the architecture of the constructed bandgap-broken heterojunctions (Fig. S4 and S5). The nature of VO-GCO interfaces, with and without intercalated amorphous carbon were further investigated by TEM and HRTEM. The images reveal the intimate interaction of their components at interfaces whatever are the heterojunctions of VO/GCO, VO/AC-P/GCO, and VO/AC-L/GCO (Figs. 1b-1g). Meanwhile, the carbon nanoparticles and carbon layer at the interfaces are amorphous. HRTEM images further exhibit the different crystal planes of  $\text{V}_2\text{O}_5$  and  $\text{GdCrO}_3$  components in constructing the bandgap-broken interfaces. The large coverage showed in the case of amorphous carbon layer indicates that VO/AC-L/GCO heterojunction experiences a larger surface contact area between the amorphous carbon and semiconductors compared to the VO/AC-P/GCO (Figs. 1e and 1g). This tightly bound and extensive surface interaction is also confirmed by elemental mapping images (Fig. S6).

The crystal structure and interaction of components for bandgap-broken heterojunctions were analyzed using XRD and Raman. The XRD spectra of  $\text{GdCrO}_3$  presents twisted perovskite structure matching with *Pbnm* space group (PDF#71-1275), and  $\text{V}_2\text{O}_5$  exhibits orthorhombic crystal structure with *Pmn21* space group (PDF#71-1275) (Fig. S7a-7c). The VO/GCO, VO/AC-P/GCO and VO/AC-L/GCO heterojunctions all show typical XRD diffraction peaks of  $\text{V}_2\text{O}_5$  and  $\text{GdCrO}_3$ . The nanoparticle or layer carbons does not exhibit diffraction peaks in XRD patterns of VO/AC-P/GCO and VO/AC-L/GCO due to the amorphous structure (Fig. S7a). Compared to  $\text{V}_2\text{O}_5$  at  $19.9^\circ$  and  $\text{GdCrO}_3$  at  $53.9^\circ$ , the heterojunctions diffraction peaks show redshifts and blueshifts, respectively, due to the strong interaction of components at interfaces severally resulting in the reduced and enlarged interplanar spacing of  $\text{V}_2\text{O}_5$  and  $\text{GdCrO}_3$  components (Fig. S7d and 7e). The strong interaction of amorphous carbon and  $\text{V}_2\text{O}_5$  at interfaces reduce the crystal crystalline of  $\text{V}_2\text{O}_5$  and result in the almost vanishing XRD peaks at  $15^\circ$ . The Raman spectra of  $\text{GdCrO}_3$  show bands in the ranges of  $100\text{--}200\text{ cm}^{-1}$  and  $200\text{--}400\text{ cm}^{-1}$ , corresponding to the vibrations of Gd atoms and Gd-O bonds, respectively (Fig. 1h) [17,18]. Additional bands above  $400\text{ cm}^{-1}$  are also observed and attributed to vibrations of the Cr-O bond in  $\text{CrO}_6$ . The Raman spectra of  $\text{V}_2\text{O}_5$  displays characteristic vibrational modes associated with its orthorhombic structure. The low-frequency region bands at  $50\text{--}800\text{ cm}^{-1}$  are primarily attributed to  $-\text{O}-\text{V}-\text{O}-\text{V}-\text{O}-$  skeleton vibrations, while the medium-high-frequency region peaks at  $992.6\text{ cm}^{-1}$  correspond to the stretching vibration of  $\text{V}=\text{O}$  [19,20]. All heterojunctions exhibit the Raman characteristic peaks of  $\text{GdCrO}_3$  and  $\text{V}_2\text{O}_5$ , except VO/AC-P/GCO and VO/AC-L/GCO, which display two new peaks at  $1383.2\text{ cm}^{-1}$  (D-band) and  $1598.9\text{ cm}^{-1}$  (G-band) assigned to the amorphous carbon [21,22]. Notably, VO/AC-L/GCO, containing a larger amount of amorphous carbon at the interface, exhibits the higher intensity of D-band and G-band compared to VO/AC-P/GCO. Furthermore, the Raman shifts of Cr-O bond of  $\text{GdCrO}_3$  at  $564.6\text{ cm}^{-1}$  and  $\text{V}=\text{O}$  bond of  $\text{V}_2\text{O}_5$  at  $992.6\text{ cm}^{-1}$  indicate the strong interactions of chemical bonds for components at interfaces (Figs. 1i and 1j). However, the Raman shifts on

VO/GCO are mitigated after introducing the amorphous carbon into VO-GCO interface to construct VO/AC-L/GCO and VO/AC-P/GCO. The attenuated Raman shifts point to the formation of Cr-O-C and V-O-C bonds at interfaces, which affects the Raman vibration of the initial Cr-O and  $\text{V}=\text{O}$  bonds for constituents in VO-AC-GCO interfaces.

The chemical bonds present at the interfaces of heterojunctions can be further analyzed by FTIR spectroscopy [23,24]. The FTIR spectra of  $\text{V}_2\text{O}_5$  exhibits three characteristic bands (Fig. S8a). A large band centered at  $530.9\text{ cm}^{-1}$  corresponding to vibration of V-O bond, and two resolved bands at  $832.9\text{ cm}^{-1}$  and  $1014.0\text{ cm}^{-1}$  may be attributed to  $\text{V}=\text{O}$  bond (Fig. S8b and 8c) [25,26]. The absorption bands of  $\text{GdCrO}_3$  at  $514.9\text{ cm}^{-1}$  are attributed to Cr-O vibrational bands, while stretching of Gd-O mode demonstrates characteristic peaks at  $580.3\text{ cm}^{-1}$  (Fig. S8d) [27]. Furthermore, the characteristic absorption band of carbon ring at  $1635.9\text{ cm}^{-1}$  was observed on FTIR spectra of the bandgap-broken heterojunction containing amorphous carbon, in agreement with the reported studies [28,29]. The combination of  $\text{V}_2\text{O}_5$  and  $\text{GdCrO}_3$  to elaborate VO/GCO heterojunction induces blueshifts (shift to higher wavenumber) of the  $\text{V}=\text{O}$  bond, while redshifts are observed for Cr-O and Gd-O bonds, compared to their individual counterparts. These observations suggest that an interaction occurs between the  $\text{V}=\text{O}$  bond and Cr-O/Gd-O bonds, leading to the formation of V-O-Gd/V-O-Cr bonds at VO-GCO interfaces. After introducing amorphous carbon (nanoparticles or layer) into the VO-GCO interface, the absorption band of  $\text{V}=\text{O}$  bond in VO/GCO ( $1013.2\text{ cm}^{-1}$ ) shift to  $1015.3\text{ cm}^{-1}$  for VO/AC-P/GCO, and to  $1016.7\text{ cm}^{-1}$  for VO/AC-L/GCO. In the meantime, the C-O bond of amorphous carbon at  $1034.7\text{ cm}^{-1}$  is shifted to lower wavenumber. The shift of FTIR absorption band points to the generation of V-O-C bond, in agreement with the Raman results. The interaction of components at VO-AC-P-GCO and VO-AC-L-GCO interfaces also results in redshifts (shift to lower wavenumber) of FTIR peaks for Cr-O and Gd-O bond in  $\text{GdCrO}_3$  and VO/GCO, implying the formation of Cr-O-C/Gd-O-C bonds at the heterojunction's interfaces. To rationalize the relationship between the shifts observed in FTIR and Raman, we compared the electronegativity of the elements. Although the electronegativity of C (2.55) is lower than O (3.44), it is significantly higher than V (1.63), Cr (1.66), and Gd (1.20). The created metal-O-C bonds (M-O-C) induce unbalanced electronegativity leading to charge transfer from metals to the carbon ring through metal-O-C bonds, which rationalizes the observed chemical shifts.

The heterojunctions were analyzed using XPS to determine the chemical surface composition and provides deep information regarding the charge interactions [30]. As shown in Fig. 2a, the O 1s XPS spectra reveal peaks centered at 530.0 eV and 529.2 eV assigned to lattice oxygen of V-O bonds in  $\text{V}_2\text{O}_5$  and Gd/Cr-O bonds in  $\text{GdCrO}_3$ , respectively [31,32]. The VO/GCO, VO/AC-P/GCO, and VO/AC-L/GCO heterojunctions all exhibit characteristic peaks of lattice oxygen for both V-O and Gd/Cr-O bonds. Furthermore, the observed peaks at 530.7 eV $\sim$ 531.4 eV for all samples correspond to O-H bond (MO-H) resulting from absorbed  $\text{H}_2\text{O}$  or hydroxyl group on the oxides surface [31,32]. The peaks of V-O bonds and Gd/Cr-O bonds in the separated oxides shift to higher energy of 530.2 eV and 529.7 eV after constructing the VO/GCO heterojunction, indicating a strong interaction between semiconductors and a charge transfer between the oxides [25]. The shifts of the V-O and Gd/Cr-O bonds are much higher once the amorphous carbon (nanoparticles or layer) is inserted between  $\text{V}_2\text{O}_5$  and  $\text{GdCrO}_3$ , pointing to the higher charge transfer thanks to the construction of M-O-C bonds (Fig. 2a). In addition, it is also supported by the deconvolution for C 1s XPS peaks of VO/AC-P/GCO and VO/AC-L/GCO, which exhibit the characteristic peak assigned to M-O-C bond at 285.7 eV (Fig. 2b). Notably, the VO/AC-L/GCO shows a higher relative amount of M-O-C bond ( $R_{\text{M-O-C/C}}$ ) (0.35) compared to VO/AC-P/GCO (0.27) due to the higher initial amount used for the carbon layer growth (Fig. 2b). In addition, the interaction between carbon atoms on carbon ring of amorphous carbon and M-O bonds of semiconductors with formatting M-O-C bonds at interfaces resulting in the blueshifts of

C=C peaks for carbon ring with respect to that of pure amorphous carbon (Fig. 2b). This matches the aforementioned redshifts of XPS peaks for M-O bonds in VO/AC-P/GCO and VO/AC-L/GCO, as compared to those of pure semiconductors, suggesting a charge shift from semiconductor components to carbon ring when V-O-C and C-O-Gd/Cr bonds on carbon ring at interfaces are formed. The charges interaction at interfaces also leads to the shifts of binding energy for Gd 2p, Cr 2p and V 2p of heterojunctions compared to semiconductor components (Fig. S9).

Based on the above HRTEM, XRD, Raman, FTIR and XPS results, it can be concluded that the incorporation of amorphous carbon into the VO-GCO interface creates chemical bonds between semiconductors and the carbon ring of amorphous carbon (V-O-(carbon ring)-O-Gd/Cr bonds) at the interface. The construction of such chemical bonds would favor the charges shifting from semiconductors to the carbon ring of amorphous carbon, resulting in a redistribution of  $\pi$  delocalized electrons within the carbon ring and benefiting to the charge separation at interfaces for photocatalytic reaction (Fig. 2c).

We have investigated the effect of M-O-C bond construction on charge and chemical bond interactions at the atomic level for heterojunctions using DFT calculations. The modes VO/AC-P/GCO and VO/AC-L/GCO heterojunctions are constructed based on the interaction region between amorphous carbon,  $V_2O_5$ , and  $GdCrO_3$  at the VO-AC-GCO interface. The DFT optimized modes of VO-AC-P-GCO and VO-AC-P-GCO interfaces are displayed (Fig. S10), suggesting that the construction of VO/AC-L/GCO and VO/AC-P/GCO heterojunction by the intercalation between amorphous carbon,  $V_2O_5$ , and  $GdCrO_3$  favors the formation of V-O-C, Cr-O-C, and Gd-O-C bonds. Clearly, the VO/AC-L/

GCO mode forms a higher amount of M-O-C bonds at the interfaces compared to VO/AC-P/GCO mode, in agreement with the experimental results. The partial density of states (PDOS) spectra for each element of the heterojunctions are also illustrated (Fig. 2d and S11). The similarity of the wavy regions on PDOS spectra suggest the formation of hybrid orbitals between the atoms. Therefore, the PDOS results indicate that the Cr-O-C, Gd-O-C and V-O-C bonds at interfaces mainly contribute from Cr 3d/O 2p/C 2p, Gd 4d/O 2p/C 2p and V 3d/O 2p/C 2p orbitals, respectively. Interestingly, the PDOS spectra further reveal that the orbital energies of V-O-C bonds (V 3d/O 2p/C 2p) and Cr-O-C bonds (Cr 3d/O 2p/C 2p) are nearly identical (Fig. 2d), indicating that charges on  $V_2O_5$  preferentially react with those on  $GdCrO_3$  aided by V-O-C and Cr-O-C bonds, respectively, at interface based on the aid of carbon ring in amorphous carbon. Moreover, the DOS spectra of amorphous carbon exhibits a faint electron peak at the Fermi level (Fig. S12a), which is associated with a low density of  $\pi$  delocalized electrons on the carbon ring [33,34]. The absence of any density at the Fermi level in pure  $GdCrO_3$  and  $V_2O_5$  suggests no delocalization of free electrons (Fig. S13). Conversely, the enhanced electrons density near the Fermi level was observed in VO/AC-P/GCO and VO/AC-L/GCO after the construction of M-O-C bonds, pointing to the charges shifting and interaction at the VO-AC-GCO heterointerfaces (Fig. S12b and 12c). In addition, VO/AC-L/GCO with a larger number of M-O-C bonds exhibits a higher density of states near the Fermi level compared to VO/AC-P/GCO, implying a more favorable charge transfer at VO-AC-L-GCO interface.

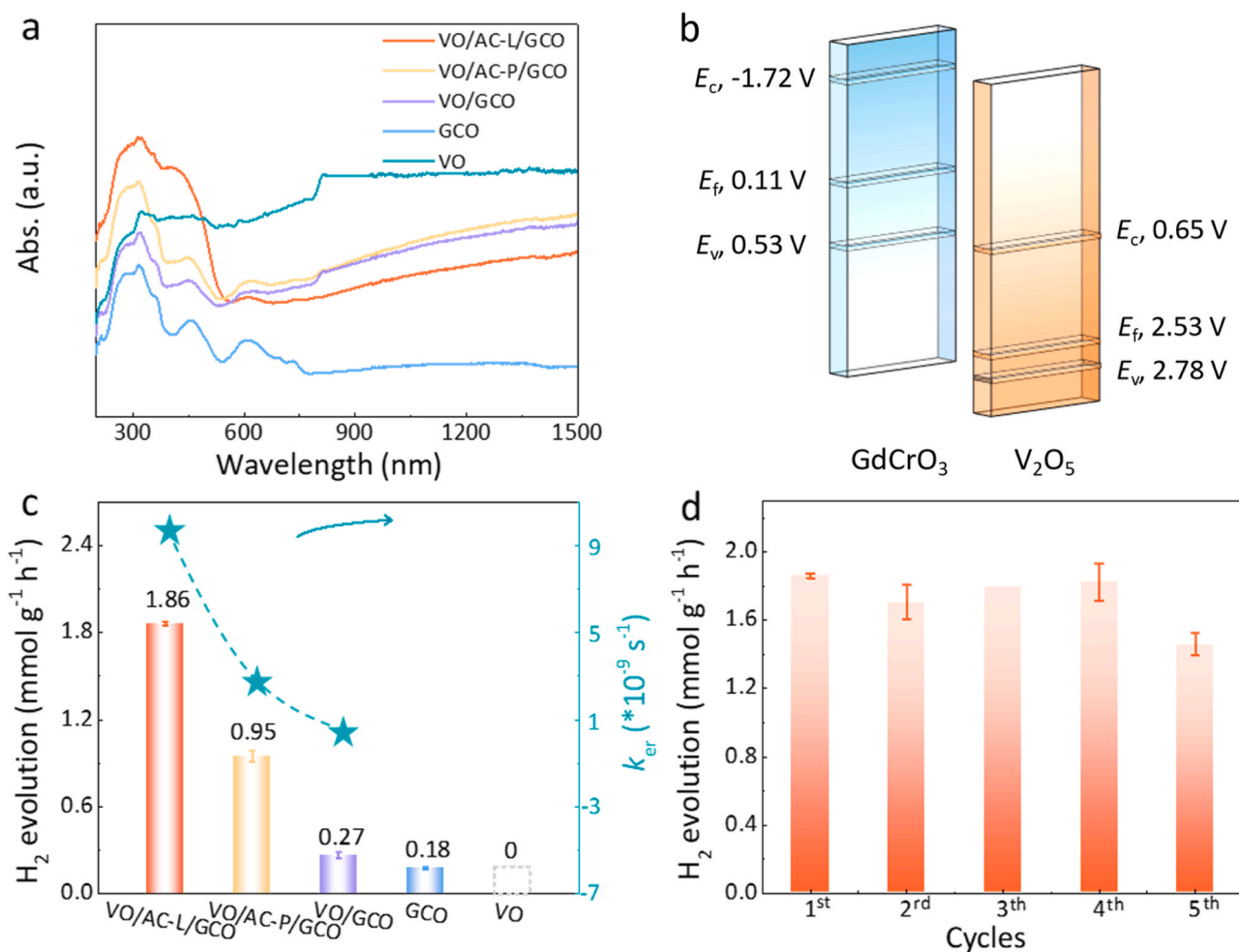


**Fig. 3.** (a) UV-Vis DRS spectra. (b) Bandgap schematic diagrams of the semiconductors. (c) Photocatalytic  $H_2$  average yielding rates and related charge transfer kinetics in heterointerfaces. (d) Photocatalytic  $H_2$  evolution cycle stability of VO/AC-L/GCO.



### 3.2. Optical property, bandgap structures and photocatalytic performance

The optical and bandgap properties of the samples were analyzed, and the results are presented. The UV-vis DRS spectra of pure  $\text{GdCrO}_3$  and  $\text{V}_2\text{O}_5$  exhibit strong visible light absorption (Fig. 3a). The near-infrared (NIR) light absorption range in  $\text{V}_2\text{O}_5$  may be mainly attributed to the collective oscillation of delocalized electrons in defects sites of surfaces, which is usually present on metal oxidizes semiconductors [35,36]. Notably, all heterojunctions VO/GCO, VO/AC-P/GCO, and VO/AC-L/GCO demonstrate semiconductor-like optical response properties with strong Vis-NIR light absorption. The bandgaps ( $E_g$ ) of  $\text{V}_2\text{O}_5$  and  $\text{GdCrO}_3$  were calculated from UV-Vis DRS spectra as 2.25 eV and 2.13 eV, according to Kubelka-Munk function method (Fig. S14). The Mott-Schottky (M-S) plots and VB-XPS measurements, commonly utilized for identifying the potential of the conduction band ( $E_c$ ), valence band ( $E_v$ ), and Fermi level ( $E_f$ ) of semiconductors, were further used to construct the band diagram of  $\text{V}_2\text{O}_5$  and  $\text{GdCrO}_3$ . The positive slopes of M-S plots indicate that both  $\text{V}_2\text{O}_5$  and  $\text{GdCrO}_3$  are *n*-type semiconductors with flat-band potentials ( $E_{fb}$ ) as 0.75 V and  $-1.62$  V (Fig. S15), respectively [37]. The  $E_c$  values of *n*-type semiconductors are

typically 0.1 V more positive than their  $E_{fb}$  values [7,38]. Therefore, the  $E_c$  and  $E_v$  values for  $\text{V}_2\text{O}_5$  (0.65 V, 2.78 V) and  $\text{GdCrO}_3$  (0.53 V,  $-1.72$  V) were determined based on their respective  $E_{fb}$  and  $E_g$  values. The PDOS spectra indicate that the  $E_v$  levels of  $\text{GdCrO}_3$  and  $\text{V}_2\text{O}_5$  are primarily associated with their O 2p/Cr 3d and O 2p orbitals (Fig. S13). Meanwhile, their  $E_c$  orbitals are predominantly associated with Cr 3d and V 3d orbitals, respectively. The VB-XPS values corresponding to the energy gap between  $E_v$  and Fermi level ( $E_f$ ) for  $\text{V}_2\text{O}_5$  and  $\text{GdCrO}_3$  are 0.42 eV and 0.25 eV, respectively (Fig. S16). Consequently, the  $E_f$  values of 2.53 V for  $\text{V}_2\text{O}_5$  and 0.11 V for  $\text{GdCrO}_3$  were calculated. In addition, Fig. 3b illustrates the band positions of semiconductors  $\text{V}_2\text{O}_5$  and  $\text{GdCrO}_3$  based on the above results, demonstrating a bandgap-broken alignment of VO/GCO with an energy barrier of 0.08 V.

The photocatalytic ability for samples was evaluated by photocatalytic hydrogen generation reaction under visible light irradiation ( $100 \text{ mW cm}^{-2}$ ). As shown in Fig. 3c, bandgap-broken VO/GCO heterojunction shows inert photocatalytic activity with an average  $\text{H}_2$  evolution rate as  $0.27 \text{ mmol g}^{-1} \text{ h}^{-1}$  due to the presence of an energy barrier at its gap-breaking interface that hinders interfacial carrier transfer. Surprisingly, the introduction of amorphous carbon into the

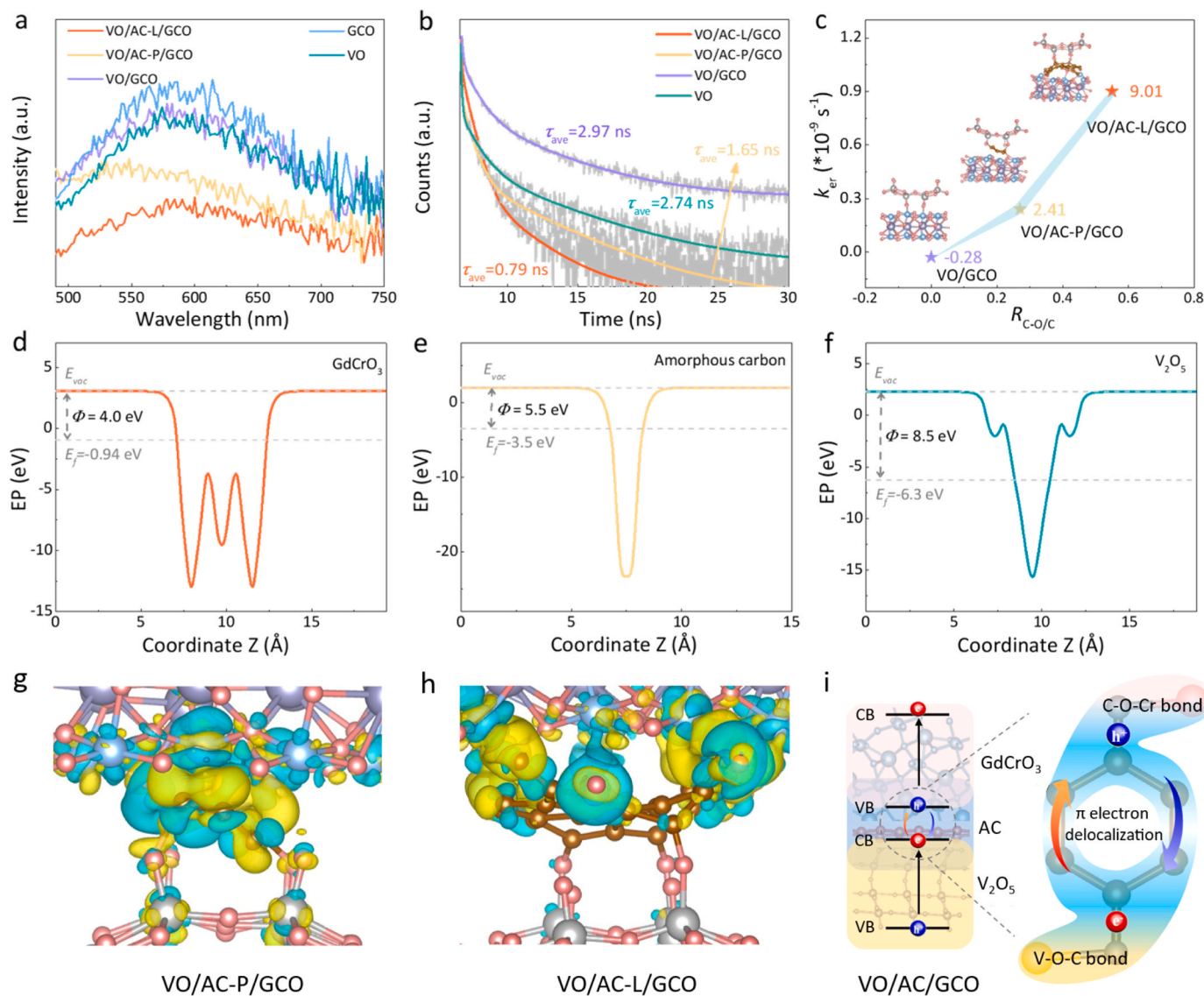


**Fig. 4.** (a) PL spectra. (b) TRPL spectra. (c) photoexcited electrons transfer rates vs. the relative amount of M-O-C bonds in interfaces of samples. (d-f) Work function of components. Differential charge density distributions in  $\text{V}_2\text{O}_5$ -AC- $\text{GdCrO}_3$  interfaces of (g) VO/AC-P/GCO and (h) VO/AC-L/GCO. (i) The photoexcited carriers transfer mechanism at VO-AC-GCO interfaces.

bandgap-broken VO-GCO interfaces leads to a significant improvement in catalytic activity, with VO/AC-P/GCO and VO/AC-L/GCO exhibiting  $H_2$  production rates of  $0.95 \text{ mmol g}^{-1} \text{ h}^{-1}$  and  $1.86 \text{ mmol g}^{-1} \text{ h}^{-1}$ , respectively. This result suggests that the higher the amount of M-O-C bonds on the heterojunction, the higher the photocatalytic properties. The  $H_2$  production rate of VO/AC-L/GCO, which has the highest amount of M-O-C bonds at interfaces, is not only 6.9 and 10.3 times higher than that of VO/GCO and pure  $GdCrO_3$ , respectively, but also comparable to most of the recently reported materials (Table S1). Moreover, VO/AC-L/GCO exhibits excellent stability in catalytic reactions with only a slight reduction in  $H_2$  yield after the fifth cycle test (Fig. 3d and S17), which may be attributed to the stable crystal structure and carbon layer protection at interfaces. No  $H_2$  gas was detected on  $V_2O_5$  because its  $E_c$  position (0.65 V vs. NEH, pH = 7) is lower than the potential required for  $H_2$  evolution reaction (−0.41 V vs. NEH, pH = 7).

### 3.3. Linkage effect in bandgap-broken interfaces by amorphous carbon for carrier transfer

In order to understand the significantly enhanced photocatalytic performance on heterojunctions after introducing amorphous carbon into bandgap-broken VO-GCO interfaces, we investigated the photoinduced charge transfer kinetics of variable samples using PL spectroscopy, and the results are depicted in Fig. 4a. The PL quenching peaks of bandgap-broken VO/GCO exhibited negligible changes compared to those of pure  $V_2O_5$  and  $GdCrO_3$ , revealing that the carriers mainly follow identical pathway of pure semiconductor due to the energy barriers at bandgap-broken interfaces [7,8,39]. The intercalation of amorphous carbon between the semiconductors to create VO-AC-P-GCO and VO-AC-L-GCO interfaces leads to fast quenching of the PL signal, which indicates lower recombination of the apparition of non-radiative events, relating to the enhanced carrier transfer in interfaces. The higher relative amount of M-O-C bonds at VO/AC-L/GCO interfaces results in the faster PL quenching and translating rapid photogenerated charge transfer with respect to VO/AC-P/GCO. Furthermore, the EIS Nyquist plots of VO/AC-L/GCO and VO/AC-P/GCO show smaller circle diameters compared to those of VO/GCO and pure semiconductors, confirming the reduction of resistance for charge transfer kinetics at interfaces when the M-O-C bonds are constructed (Fig. S18) [40]. To track the charge transfer kinetics from  $V_2O_5$  to  $GdCrO_3$  before and after the construction of M-O-C bonds, the time resolved PL (TRPL) spectra of samples were tested and fitted (Fig. 4b). The average lifetime extracted from TRPL spectra of  $V_2O_5$  exhibit an average lifetime ( $\tau_{ave}$ ) of 2.74 ns. The energy barriers at bandgap-broken interfaces hindering charge transfer from  $E_c$  of  $V_2O_5$  to  $E_v$  of  $GdCrO_3$ , resulting in a higher  $\tau_{ave}$  of 2.97 ns for VO/GCO. Nevertheless, the  $\tau_{ave}$  values for VO/AC-P/GCO (1.65 ns) and VO/AC-L/GCO (0.79 ns) are significantly lower compared to that of  $V_2O_5$  after introduced M-O-C bonds into VO-GCO interfaces, enhancing the charge migration. The electron transfer rates ( $k_{er}$ ) in interfaces were calculated using Eq. (4) [9,16].

$$k_{er} = 1/\tau_{ave}(\text{heterojunction}) - 1/\tau_{ave}(\text{semiconductor}) \quad (4)$$

where  $\tau_{ave}$  (heterojunction) corresponds to  $\tau_{ave}$  of VO/GCO, VO/AC-P/GCO or VO/AC-L/GCO.  $\tau_{ave}$  (semiconductor) refers to  $\tau_{ave}$  of  $V_2O_5$ . The calculated  $k_{er}$  value for VO/AC-L/GCO is  $9.01 \times 10^{-8} \text{ s}^{-1}$ , which is significantly higher than that of VO/AC-P/GCO ( $2.41 \times 10^{-8} \text{ s}^{-1}$ ) and VO/GCO ( $-0.28 \times 10^{-8} \text{ s}^{-1}$ ). This suggests that the created V-O-C and Cr-O-C bonds serve as charge transfer bridges, linking bandgap-broken VO-GCO interfaces to achieve quick charge transfer. Fig. 4c illustrates the correlation between the  $k_{er}$  of heterojunctions and the relative amount of M-O-C bonds extracted from XPS analysis. The  $k_{er}$  promote increase as the relative amount of M-O-C bonds at bandgap-broken increase, further confirming the effective role in constructing M-O-C bonds as facilitator for charge transfer at the bandgap-broken VO-GCO interface. The improved charge separation efficiency of VO/AC-P/GCO and

VO/AC-L/GCO is translated by a higher photocurrent density compared to VO/GCO and pure semiconductors (Fig. S19). However, VO+AC+GCO physical mixture without M-O-C bonds at interface shows almost equal photocurrent density to bandgap-broken VO/GCO heterojunction. Obviously, the photocatalytic hydrogen generation rates of heterojunctions are positively related to carriers transfer kinetics ( $k_{er}$ ) in interfaces (Fig. 3c). The higher  $k_{er}$  of heterojunction achieves more concentration of carriers on surfaces in photocatalytic hydrogen production reaction, which is verified by the lower slopes of M-S plots (Fig. S20) [41,42].

We investigated the charge density distribution of bandgap-broken heterojunction after the insertion of variable amount of M-O-C bonds to gain a deeper understanding of the charge transfer properties (Fig. S10). The work functions were extracted from the average potential profile along the  $z$  axis of  $GdCrO_3$ , amorphous carbon, and  $V_2O_5$ , to be 4.0 eV, 5.5 eV, and 8.5 eV, respectively (Figs. 4d–4f). The calculated Fermi levels is 0.94 eV ( $GdCrO_3$ ), −3.5 eV (amorphous carbon), and −6.3 eV ( $V_2O_5$ ), in agreement with experimental Fermi level order ( $GdCrO_3 > V_2O_5$ ). The three-dimensional charge density of bandgap-broken heterojunctions VO/AC-P/GCO, VO/AC-L/GCO, and VO/GCO are displayed (Figs. 4g, 4h and S21), in which the yellow region refers to electron accumulation (electrons) and the cyan one to depletion (holes). Theoretically, due to the high work function in  $V_2O_5$  and the low Fermi level in  $GdCrO_3$ , an electron transfer from  $GdCrO_3$  to  $V_2O_5$  is expected at the VO/GCO heterojunction. In this disposition, the charge transfer from  $V_2O_5$  to  $GdCrO_3$  at interface is less likely, hindered by energy barriers in bandgap-broken VO-GCO interfaces. Remarkably, the charge interactions (yellow and cyan regions) at the interfaces of VO/AC-P/GCO and VO/AC-L/GCO heterojunctions are significantly enhanced compared to those of VO/GCO upon introducing amorphous carbon into the bandgap-broken VO-GCO interfaces. The charge interactions are evidently dependent on the M-O-C bonds present on the carbon ring of amorphous carbon. The higher amount of M-O-C bonds shows the larger total charge interaction areas (Fig. S22). Therefore, the charge transfer at bandgap-broken VO-GCO interfaces can be precisely regulated by controlling the amount of M-O-C bonds (or interaction areas in VO-amorphous carbon-GCO interfaces) at interface, matching well with the above experimental PL and TRPL results. The interacted charges at interfaces can be further demonstrated by planar-averaged electron density difference of VO-AC-L-GCO interface, in which electrons transfer from  $V_2O_5$  to recombine with holes in  $GdCrO_3$  via the redistributed and dissipative of  $\pi$  electron delocalization in carbon ring of amorphous carbon at interface, leaving free electrons on  $GdCrO_3$  and holes on  $V_2O_5$  for photocatalytic reactions (Fig. S23).

According to the above experimental and theoretical results, a linkage effect is induced by amorphous carbon in interfaces of bandgap-broken heterojunctions for photocatalytic hydrogen production reaction. Firstly, the incorporation of amorphous carbon and semiconductors in bandgap-broken VO-GCO interfaces generate Cr-O-C and V-O-C bonds with Cr 3d/O 2p/C 2p orbitals and V 3d/O 2p/C 2p orbitals, respectively, with almost equal energies. Then, these hybrid orbitals overcome the gap-breaking energy barriers in VO-GCO interfaces and induce the photoexcited holes on  $E_v$  (Cr 3d/O 2p orbitals) for  $GdCrO_3$  and electrons on  $E_c$  (V 3d orbital) for  $V_2O_5$  migrate to amorphous carbon through Cr-O-C bond and V-O-C bond at interface under light irradiation. These holes and electrons subsequently recombine via the redistributed and dissipative of  $\pi$  electron delocalization in carbon ring of amorphous, leaving free photoexcited electrons on  $E_c$  of  $GdCrO_3$  and holes on  $E_v$  of  $V_2O_5$  for photocatalytic reactions (Fig. 4i). In this way, the constructed bandgap-broken VO/AC-P/GCO and VO/AC-L/GCO heterojunctions enable carrier migration and separation and hence optimized photocatalytic performance for hydrogen production compared to VO/GCO.



### 3.4. The linkage effect in carbon allotropes-based bandgap-broken heterojunctions

In order to further evaluate the universality of linkage effect derived from conjugated carbons in the bandgap-broken VO-GCO interfaces in photocatalytic hydrogen production, different carbon allotropes, graphene (GN), carbon nanotube (CNT), graphdiyne (GDY) were introduced into VO-GCO interfaces to construct a series of bandgap-broken heterojunctions as VO/GN/GCO, VO/CNT/GCO and VO/GDY/GCO. The TEM/HRTEM, XRD, FTIR, and XPS measurements verify the successful synthesis of these heterojunctions and the created metal-O-C bond (V-O-C and Cr-O-C bonds) in their interfaces (Fig. S24-S29). The PL and TRPL spectra of the above carbon allotropes-based heterojunctions were carried out to analyze the charge transfer kinetics in bandgap-broken interfaces (Figs. 5a-5c, and S30). The lower PL quenching peaks for VO/GN/GCO, VO/CNT/GCO and VO/GDY/GCO compared to  $\text{V}_2\text{O}_5$  and  $\text{GdCrO}_3$  suggest the enhanced carrier migration at interfaces with the assistance of metal-O-C bond. These lead to the significantly lower  $\tau_{\text{ave}}$  values of VO/GN/GCO (1.77 ns), VO/CNT/GCO (1.01 ns) and VO/GDY/GCO (1.56 ns) obtained from fitting TRPL spectra with respect to 2.74 ns of  $\text{V}_2\text{O}_5$ . Furthermore, the photoexcited electrons transfer rates ( $k_{\text{er}}$ ) of VO/GN/GCO ( $1.99 \times 10^8 \text{ s}^{-1}$ ), VO/CNT/GCO ( $6.25 \times 10^8 \text{ s}^{-1}$ ) and VO/GDY/GCO ( $2.76 \times 10^8 \text{ s}^{-1}$ ) were calculated according to  $\tau_{\text{ave}}$  values, indicating efficient carrier transfer from

$\text{V}_2\text{O}_5$  to  $\text{GdCrO}_3$  in bandgap-broken interfaces linking by the metal-O-C bond in a series of conjugated carbons rings of carbon allotropes. Therefore, the photocatalytic  $\text{H}_2$  evolution rates of VO/GN/GCO ( $1.03 \text{ mmol g}^{-1} \text{ h}^{-1}$ ), VO/CNT/GCO ( $1.59 \text{ mmol g}^{-1} \text{ h}^{-1}$ ), VO/GDY/GCO ( $1.15 \text{ mmol g}^{-1} \text{ h}^{-1}$ ) are all markedly higher than the bandgap-broken VO/GCO ( $0.27 \text{ mmol g}^{-1} \text{ h}^{-1}$ ) and pure  $\text{GdCrO}_3$  ( $0.18 \text{ mmol g}^{-1} \text{ h}^{-1}$ ) (Fig. S31).

In order to divide the effect of work functions (WF) and impedance ( $R_{\text{ct}}$ ) of carbon allotropes, and the relative amount of M-O-C bond ( $R_{\text{M-O-C/C}}$ ) at interfaces for charge transfer kinetics ( $k_{\text{er}}$ ) and photocatalytic  $\text{H}_2$  evolution rate ( $\text{mmol g}^{-1} \text{ h}^{-1}$ ) of carbon-based bandgap-broken heterojunctions, a radar map summarizing the above factors is summarized (Fig. 5d, S32 and Table S2). Although the GN shows the highest electric conductivity with the lowest  $R_{\text{ct}}$  value, the  $k_{\text{er}}$  value of VO/GN/GCO ( $1.99 \times 10^8 \text{ s}^{-1}$ ) is lower than VO/CNT/GCO ( $6.25 \times 10^8 \text{ s}^{-1}$ ) and VO/GDY/GCO ( $2.76 \times 10^8 \text{ s}^{-1}$ ) (Fig. 5d). In addition, the WF value of GDY (5.38 eV) is higher than 4.89 eV of CNT, while its  $k_{\text{er}}$  value is lower than that of VO/CNT/GCO. These results imply that neither WF nor electric conductivity ( $R_{\text{ct}}$  values) of carbon allotropes are the key factor to improve photoexcited charge transfer at bandgap-broken VO-GCO interfaces. However, with increasing the relative amount of M-O-C bond in heterojunctions, the  $k_{\text{er}}$  values increase with an order as: VO/AC-L/GCO > VO/CNT/GCO > VO/GDY/GCO > VO/GN/GCO. The photocatalytic  $\text{H}_2$  evolution rate of these carbon allotrope-based

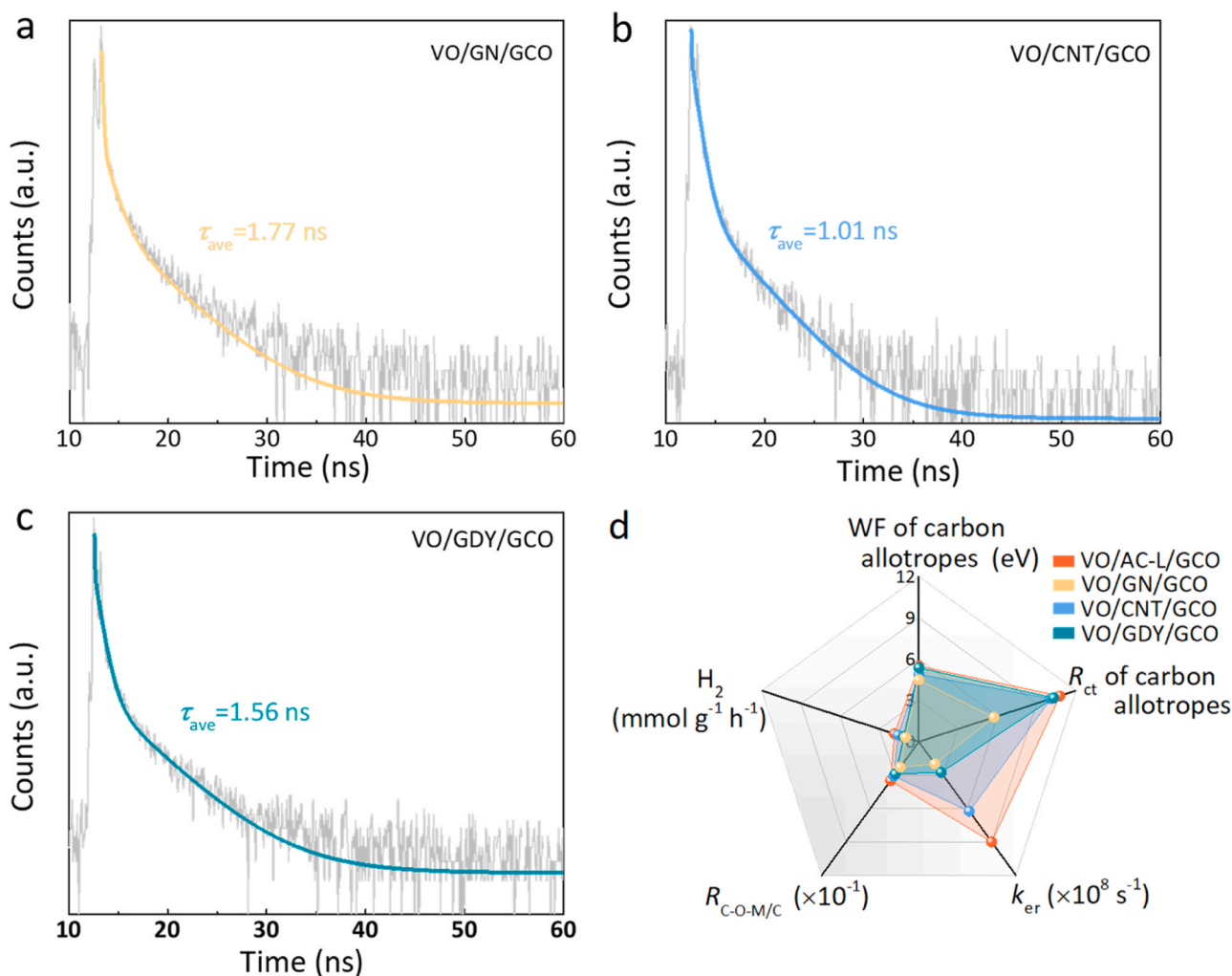


**Fig. 5.** TRPL spectra of (a) VO/GN/GCO, (b) VO/CNT/GCO, (c) VO/GDY/GCO. (d) The radar map of samples, including parameters for work functions (WF) and  $R_{\text{ct}}$  values of carbon allotropes, the relative amount of M-O-C bonds ( $R_{\text{M-O-C/C}}$ ) in heterojunctions, photoexcited electron transfer rates ( $k_{\text{er}}$ ) and  $\text{H}_2$  generation rates of heterojunctions.

heterojunctions also increases on the order of the above  $k_{\text{er}}$  values. Compared to VO/GN/GCO, VO/CNT/GCO, and VO/GDY/GCO, the VO/AC-L/GCO has the highest amount of metal-O-C bonds and  $k_{\text{er}}$  value in bandgap-broken VO-GCO interfaces. Accordingly, the VO/AC-L/GCO has the highest carrier separation efficiency and showing the highest photocatalytic hydrogen production performance. The all above results suggest that the charge transfer kinetics and photocatalytic hydrogen production performance of bandgap-broken heterojunctions can be precisely regulated by controlling the amount of metal-O-C bonds in carbon allotropes-based bandgap-broken interfaces.

#### 4. Conclusion

In summary, we construct bandgap-broken heterojunctions VO/AC-L/GCO and VO/AC-P/GCO by introducing the amorphous carbon into the VO-GCO interfaces. The amorphous carbon at interface creates a linkage effect in heterojunctions for photocatalytic hydrogen production reactions. The as-designed VO/AC-L/GCO has abundant M-O-C bonds to assist carrier migration and separation at bandgap-broken interfaces, thereby shows excellent photocatalytic hydrogen production rate as high as  $1.86 \text{ mmol g}^{-1} \text{ h}^{-1}$ , which is 6.9 times higher than VO/GCO. Furthermore, substituting the amorphous carbon by the other carbon allotropes, graphene (GN), carbon nanotube (CNT), and graphdiyne (GDY), to construct a series of bandgap-broken heterojunctions VO/GN/GCO, VO/CNT/GCO and VO/GDY/GCO, the optimized charge transfer kinetics and high photocatalytic hydrogen yielding rates ( $0.78\text{--}1.59 \text{ mmol g}^{-1} \text{ h}^{-1}$ ) have been also achieved. This work demonstrates a universal strategy to introducing the carbon allotropes-based metal-O-C bonds into bandgap-broken interface to assist the charge transfer, which can open a pathway to activate the bandgap-broken heterojunction in photo(electro)catalytic applications.

#### CRediT authorship contribution statement

**Prof. Z.-Q. Liu** conceived and designed the project, **J. Li, Z. Huang, C. Wang, L. Tian, X. Yang, R. Zhou**, and **M. N. Ghazzal** performed the experiments and carried out the DFT calculations, **J. Li** and **Z. Q. Liu** analyzed the data, wrote and revised the article.

#### Declaration of Competing Interest

The authors declare that they have no known competing financial interests or personal relationships that could have appeared to influence the work reported in this paper.

#### Data availability

Data will be made available on request.

#### Acknowledgments

This work was financially supported by the Natural Science Foundation of China (No. 22278094), Outstanding Youth Project of Guangdong Natural Science Foundation (No. 2020B1515020028), Guangdong Natural Science Foundation (No. 2021A1515010066), University Innovation Team Scientific Research Project of Guangzhou Education Bureau (No. 202235246). CW and MNG acknowledges the funding provided by the French National Research Agency (ANR), through the IngenCat project (ANR-20-CE43-0014) and ACT programme (NEXT-CUS project ID: 327327).

#### Appendix A. Supporting information

Supplementary data associated with this article can be found in the online version at [doi:10.1016/j.apcatb.2023.123181](https://doi.org/10.1016/j.apcatb.2023.123181).

#### References

- [1] H. Wang, L. Zhang, Z. Chen, J. Hu, S. Li, Z. Wang, J. Liu, X. Wang, Semiconductor heterojunction photocatalysts: design, construction, and photocatalytic performances, *Chem. Soc. Rev.* 43 (2014) 5234–5244, <https://doi.org/10.1039/C4CS00126E>.
- [2] Q. Xu, L. Zhang, B. Cheng, J. Fan, J. Yu, S-scheme heterojunction photocatalyst, *Chem* 6 (2020) 1543–1559, <https://doi.org/10.1016/j.chempr.2020.06.010>.
- [3] J. Low, J. Yu, M. Jaroniec, S. Wageh, A.A. Al-Ghamdi, Heterojunction photocatalysts, *Adv. Mater.* 29 (2017), 1601694, <https://doi.org/10.1002/adma.201601694>.
- [4] H. Chih-Wei, F. Ming-Long, V.P.-H. Hu, S. Pin, Investigation and simulation of work-function variation for III–V broken-gap heterojunction tunnel FET, *IEEE J. Electron Dev.* 3 (2015) 194–199, <https://doi.org/10.1109/jeds.2015.2408356>.
- [5] C. Tan, S. Yin, J. Chen, Y. Lu, W. Wei, H. Du, K. Liu, F. Wang, T. Zhai, L. Li, Broken-gap PtS<sub>2</sub>/WSe<sub>2</sub> van der waals heterojunction with ultrahigh reverse rectification and fast photoresponse, *ACS Nano* 15 (2021) 8328–8337, <https://doi.org/10.1021/acsnano.0c09593>.
- [6] P.K. Srivastava, Y. Hassan, Y. Gebredingle, J. Jung, B. Kang, W.J. Yoo, B. Singh, C. Lee, Multifunctional van der waals broken-gap heterojunction, *Small* 15 (2019), 1804885, <https://doi.org/10.1002/sml.201804885>.
- [7] J. Li, X. Yang, C. Ma, Y. Lei, Z. Cheng, Z. Rui, Selectively recombining the photoinduced charges in bandgap-broken Ag<sub>3</sub>PO<sub>4</sub>/GdCrO<sub>3</sub> with a plasmonic Ag bridge for efficient photothermocatalytic VOCs degradation and CO<sub>2</sub> reduction, *Appl. Catal. B: Environ.* 291 (2021), 120053, <https://doi.org/10.1016/j.apcatb.2021.120053>.
- [8] J. Li, J. Feng, X. Guo, H. Fang, J. Chen, C. Ma, R. Li, Y. Wang, Z. Rui, Defect-band bridge photothermally activates Type III heterojunction for CO<sub>2</sub> reduction and typical VOCs oxidation, *Appl. Catal. B Environ.* 309 (2022), <https://doi.org/10.1016/j.apcatb.2022.121248>.
- [9] J. Li, H. Fang, M. Wu, C. Ma, R. Lian, S.P. Jiang, M.N. Ghazzal, Z. Rui, Selective cocatalytic decoration of narrow-bandgap broken-gap heterojunction for directional charge transfer and high photocatalytic properties, *Small* (2023), e2300559, <https://doi.org/10.1002/sml.202300559>.
- [10] R. Shen, L. Zhang, N. Li, Z. Lou, T. Ma, P. Zhang, Y. Li, X. Li, W–N bonds precisely boost Z-scheme interfacial charge transfer in g-C<sub>3</sub>N<sub>4</sub>/WO<sub>3</sub> heterojunctions for enhanced photocatalytic H<sub>2</sub> evolution, *ACS Catal.* 12 (2022) 9994–10003, <https://doi.org/10.1021/acscatal.2c02416>.
- [11] Z. Zhao, Z. Wang, J. Zhang, C. Shao, K. Dai, K. Fan, C. Liang, Interfacial chemical bond and oxygen vacancy-enhanced In<sub>2</sub>O<sub>3</sub>/CdSe-DETA S-scheme heterojunction for photocatalytic CO<sub>2</sub> conversion, *Adv. Funct. Mater.* (2023), 2214470, <https://doi.org/10.1002/adfm.202214470>.
- [12] J. Zhao, M. Ji, H. Chen, Y.-X. Weng, J. Zhong, Y. Li, Y. Li, Z. Chen, J. Xia, H. Li, Interfacial chemical bond modulated Bi<sub>19</sub>S<sub>27</sub>Br<sub>3</sub>/g-C<sub>3</sub>N<sub>4</sub> Z-scheme heterojunction for enhanced photocatalytic CO<sub>2</sub> conversion, *Appl. Catal. B: Environ.* 307 (2022), 121162, <https://doi.org/10.1016/j.apcatb.2022.121162>.
- [13] F. Hasanvandian, A. Shokri, M. Moradi, B. Kakavandi, S. Rahman Setayesh, Encapsulation of spinel CuCo<sub>2</sub>O<sub>4</sub> hollow sphere in V<sub>2</sub>O<sub>5</sub>-decorated graphitic carbon nitride as high-efficiency double Z-type nanocomposite for levofloxacin photodegradation, *J. Hazard. Mater.* 423 (2022), 127090, <https://doi.org/10.1016/j.jhazmat.2021.127090>.
- [14] S. Le, C. Zhu, Y. Cao, P. Wang, Q. Liu, H. Zhou, C. Chen, S. Wang, X. Duan, V<sub>2</sub>O<sub>5</sub> nanodot-decorated laminar C<sub>3</sub>N<sub>4</sub> for sustainable photodegradation of amoxicillin under solar light, *Appl. Catal. B: Environ.* 303 (2022), 120903, <https://doi.org/10.1016/j.apcatb.2021.120903>.
- [15] J. Li, A. Slassi, X. Han, D. Cornil, M.H. Ha-Thi, T. Pino, D.P. Debecker, C. Colbeau-Justin, J. Arbiol, J. Cornil, M.N. Ghazzal, Tuning the electronic bandgap of graphdiyne by H-substitution to promote interfacial charge carrier separation for enhanced photocatalytic hydrogen production, *Adv. Funct. Mater.* 31 (2021), 2100994, <https://doi.org/10.1002/adfm.202100994>.
- [16] J. Li, J. Chen, H. Fang, X. Guo, Z. Rui, Plasmonic metal bridge leading Type III heterojunctions to robust Type B photothermocatalysts, *Ind. Eng. Chem. Res.* 60 (2021) 8420–8429, <https://doi.org/10.1021/acs.iecr.1c01198>.
- [17] H. Hu, Y. Su, C. Shi, G. Gong, J. Zhou, Y. Wang, Influence of particle size on the magnetocaloric and dielectric properties of GdCrO<sub>3</sub>, *J. Mater. Sci. Mater. El* 33 (2022) 12113–12125, <https://doi.org/10.1007/s10854-022-08171-3>.
- [18] A.A.A. Qahtan, S. Husain, A. Somvanshi, W. Khan, Y.K. Manea, Influence of Mn doping on dielectric properties, conduction mechanism and photocatalytic nature of gadolinium-based orthochromites, *J. Mater. Sci. Mater. El* 31 (2020) 9335–9351, <https://doi.org/10.1007/s10854-020-03474-9>.
- [19] Z. Zhang, W. Xie, J. Li, H. Zhang, Q. Wang, C. Zhang, G. Xu, J. Gao, A.A. Rogachev, H. Cao, In situ raman observation of dynamically structural transformation induced by electrochemical lithium intercalation and deintercalation from multi-electrochromic V<sub>2</sub>O<sub>5</sub> thin films, *Adv. Mater. Interfaces* 9 (2022), 2200883, <https://doi.org/10.1002/admi.202200883>.
- [20] J. Song, S. Impeng, J. Zhang, J. Deng, D. Zhang, Elucidating the sensitivity of vanadyl species to water over V<sub>2</sub>O<sub>5</sub>/TiO<sub>2</sub> catalysts for NO<sub>x</sub> abatement via operando Raman spectroscopy, *J. Catal.* 416 (2022) 198–208, <https://doi.org/10.1016/j.jcat.2022.11.003>.
- [21] C. Liang, Y. Chen, M. Wu, K. Wang, W. Zhang, Y. Gan, H. Huang, J. Chen, Y. Xia, J. Zhang, S. Zheng, H. Pan, Green synthesis of graphite from CO<sub>2</sub> without graphitization process of amorphous carbon, *Nat. Commun.* 12 (2021) 119, <https://doi.org/10.1038/s41467-020-20380-0>.
- [22] W.A. Wang, H. Huang, B. Wang, C. Qian, P. Li, J. Zhou, Z. Liang, C. Yang, S. Guo, A new dual-ion battery based on amorphous carbon, *Sci. Bull.* 64 (2019) 1634–1642, <https://doi.org/10.1016/j.scib.2019.08.021>.

- [23] X. Zhang, J. Yan, F. Zheng, J. Zhao, L.Y.S. Lee, Designing charge transfer route at the interface between WP nanoparticle and g-C<sub>3</sub>N<sub>4</sub> for highly enhanced photocatalytic CO<sub>2</sub> reduction reaction, *Appl. Catal. B: Environ.* 286 (2021), 119385, <https://doi.org/10.1016/j.apcatb.2021.119879>.
- [24] J. Shi, F. Chen, L. Hou, G. Li, Y. Li, X. Guan, H. Liu, L. Guo, Eosin Y bidentately bridged on UiO-66-NH<sub>2</sub> by solvothermal treatment towards enhanced visible-light-driven photocatalytic H<sub>2</sub> production, *Appl. Catal. B: Environ.* 280 (2021), 119879, <https://doi.org/10.1016/j.apcatb.2020.119385>.
- [25] S. Sasidharan, S.V. Sasidharan Nair, A. Sudhakaran, R. Sreenivasan, Insight into the fabrication and characterization of novel heterojunctions of Fe<sub>2</sub>O<sub>3</sub> and V<sub>2</sub>O<sub>5</sub> with TiO<sub>2</sub> and graphene oxide for enhanced photocatalytic hydrogen evolution: a comparison study, *Ind. Eng. Chem. Res.* 61 (2022) 2714–2733, <https://doi.org/10.1021/acs.iecr.1c04437>.
- [26] T. Liu, L. Chen, X. Wang, Y. Huang, M. Wang, Y. Zhang, Polypyrrole-coated V<sub>2</sub>O<sub>5</sub> nanobelts arrays on carbon cloth for high performance zinc energy storage, *Electrochim. Acta* 441 (2023), 141806, <https://doi.org/10.1016/j.electacta.2022.141806>.
- [27] Y. Jia, J. Li, Z. Liu, Q. Wang, W. Zhang, J.-S. Bae, C. Liu, Pt-GdCrO<sub>3</sub>-Bi<sub>2</sub>MoO<sub>6</sub> ternary heterojunction with high photocatalytic activities for CO<sub>2</sub> reduction and water purification, *Chem. Eng. J.* 437 (2022), 135300, <https://doi.org/10.1016/j.cej.2022.135300>.
- [28] J. Jiang, W. Yang, Y. Cheng, Z. Liu, Q. Zhang, K. Zhao, Molecular structure characterization of middle-high rank coal via XRD, Raman and FTIR spectroscopy: implications for coalification, *Fuel* 239 (2019) 559–572, <https://doi.org/10.1016/j.fuel.2018.11.057>.
- [29] P.M. Anjana, M.R. Bindhu, M. Umadevi, R.B. Rakhi, Antibacterial and electrochemical activities of silver, gold, and palladium nanoparticles dispersed amorphous carbon composites, *Appl. Surf. Sci.* 479 (2019) 96–104, <https://doi.org/10.1016/j.apsusc.2019.02.057>.
- [30] Z.-K. Shen, M. Cheng, Y.-J. Yuan, L. Pei, J. Zhong, J. Guan, X. Li, Z.-J. Li, L. Bao, X. Zhang, Z.-T. Yu, Z. Zou, Identifying the role of interface chemical bonds in activating charge transfer for enhanced photocatalytic nitrogen fixation of Ni<sub>2</sub>P-black phosphorus photocatalysts, *Appl. Catal. B: Environ.* 295 (2021), 120274, <https://doi.org/10.1016/j.apcatb.2021.120274>.
- [31] S. Li, N. Hasan, H. Ma, G. Zhu, L. Pan, F. Zhang, N. Son, M. Kang, C. Liu, Hierarchical V<sub>2</sub>O<sub>5</sub>/ZnV<sub>2</sub>O<sub>6</sub> nanosheets photocatalyst for CO<sub>2</sub> reduction to solar fuels, *Chem. Eng. J.* 430 (2022), <https://doi.org/10.1016/j.cej.2021.132863>.
- [32] A. Nashim, S. Pany, K.M. Parida, Systematic investigation on the charge storage behavior of GdCrO<sub>3</sub> in aqueous electrolyte, *J. Energy Storage* 42 (2021), 103145, <https://doi.org/10.1016/j.est.2021.103145>.
- [33] J. Robertson, Amorphous carbon, *Adv. Phys.* 35 (1986) 317–374, <https://doi.org/10.1080/00018738600101911>.
- [34] C. Bie, H. Yu, B. Cheng, W. Ho, J. Fan, J. Yu, Design, fabrication, and mechanism of nitrogen-doped graphene-based photocatalyst, *Adv. Mater.* 33 (2021), 2003521, <https://doi.org/10.1002/adma.202003521>.
- [35] C. Lu, X. Li, Q. Wu, J. Li, L. Wen, Y. Dai, B. Huang, B. Li, Z. Lou, Constructing surface plasmon resonance on Bi<sub>2</sub>WO<sub>6</sub> to boost high-selective CO<sub>2</sub> reduction for methane, *ACS Nano* 15 (2021) 3529–3539, <https://doi.org/10.1021/acsnano.1c00452>.
- [36] L. Hao, H. Huang, Y. Zhang, T. Ma, Oxygen vacant semiconductor photocatalysts, *Adv. Funct. Mater.* 31 (2021), 2100919, <https://doi.org/10.1002/adfm.202100919>.
- [37] X. Tao, H. Zhou, C. Zhang, N. Ta, R. Li, C. Li, Triclinic-phase bismuth chromate: a promising candidate for photocatalytic water splitting with broad spectrum ranges, *Adv. Mater.* 35 (2023), 2211182, <https://doi.org/10.1002/adma.202211182>.
- [38] K. Liu, R. Cui, Z. Liu, S. Yao, S. Sun, J. Ma, R.-C. Sun, Fractional thermal reduction of CuInS<sub>2</sub> quantum dot-sensitized Bi<sub>2</sub>MoO<sub>6</sub> hierarchical flowers on S-doped biochar for dual Z-scheme/mott-schottky heterojunction construction: a strategy for efficient photocatalytic biorefineries, *ACS Sustain. Chem. Eng.* 11 (2023) 5400–5407, <https://doi.org/10.1021/acssuschemeng.2c06572>.
- [39] X. Ruan, C. Huang, H. Cheng, Z. Zhang, Y. Cui, Z. Li, T. Xie, K. Ba, H. Zhang, L. Zhang, X. Zhao, J. Leng, S. Jin, W. Zhang, W. Zheng, S.K. Ravi, Z. Jiang, X. Cui, J. Yu, A twin S-scheme artificial photosynthetic system with self-assembled heterojunctions yields superior photocatalytic hydrogen evolution rate, *Adv. Mater.* 35 (2023), 2209141, <https://doi.org/10.1002/adma.202209141>.
- [40] Z. Yang, M. Li, S. Chen, S. Yang, F. Peng, J. Liao, Y. Fang, S. Zhang, S. Zhang, Cocatalyst engineering with robust tunable carbon-encapsulated Mo-rich Mo/Mo<sub>2</sub>C heterostructure nanoparticle for efficient photocatalytic hydrogen evolution, *Adv. Funct. Mater.* 33 (2023), 2212746, <https://doi.org/10.1002/adfm.202212746>.
- [41] J. Yuan, Y. Tang, X. Yi, C. Liu, C. Li, Y. Zeng, S. Luo, Crystallization, cyanamide defect and ion induction of carbon nitride: exciton polarization dissociation, charge transfer and surface electron density for enhanced hydrogen evolution, *Appl. Catal. B: Environ.* 251 (2019) 206–212, <https://doi.org/10.1016/j.apcatb.2019.03.069>.
- [42] S. Feng, T. Wang, B. Liu, C. Hu, L. Li, Z.J. Zhao, J. Gong, Enriched surface oxygen vacancies of photoanodes by photoetching with enhanced charge separation, *Angew. Chem. Int. Ed.* 59 (2020) 2044–2048, <https://doi.org/10.1002/anie.201913295>.